

Supporting Information

Jackson et al. 10.1073/pnas.0907548106

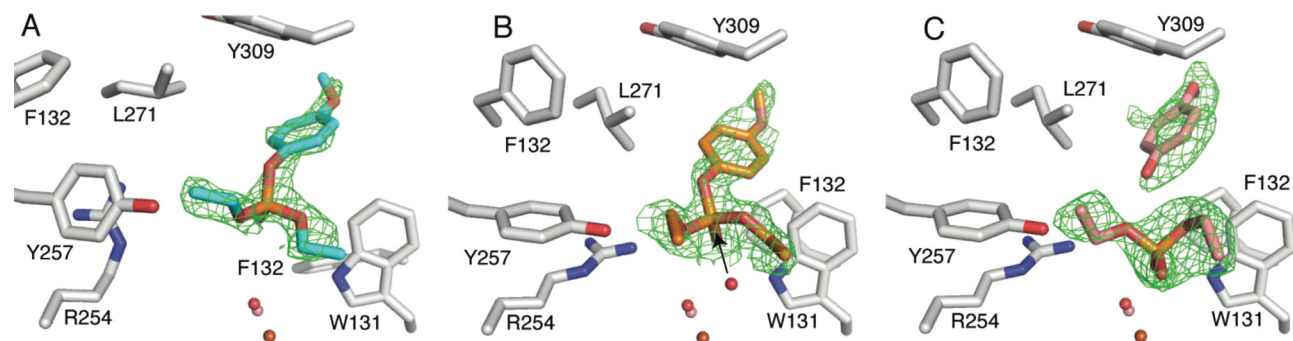


Fig. S1. Crystal structures of *arPTE* $E_{open}S$, $E_{closed}S$, and EP complexes. Electron density $f_o - f_c$ omit maps are represented by green mesh contoured at 3.0σ . The structure of the $E_{open}S$ complex in which the substrate is 4.0 Å from the β -metal ion is shown in (A). This structure is of the *arPTE* 8M variant (3A3W), which is predominantly in the E_{open} conformation. (B) The $E_{closed}S$ complex with the substrate 3.3 Å from the β -metal ion is shown as well as the proposed position of the nucleophilic water. Closer contacts with the immediate active site (F132, R254, Y257, L271) are evident. This structure is of the wild-type *arPTE* enzyme (2RIN). The EP complex, with the diethyl phosphate product 2.4 Å from the β -metal ion is shown in (C). Again, this structure is of the wild-type enzyme (2RIN).

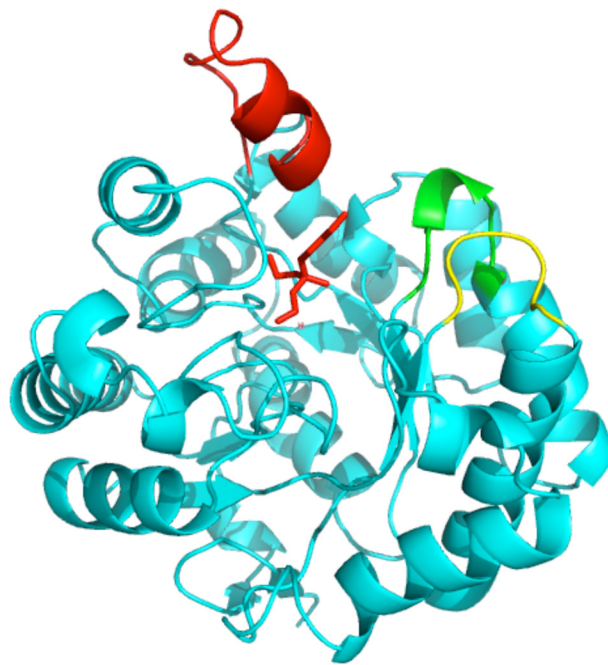


Fig. S2. The positions of mobile loops in the PTEs. Loops 7 (red; 256–274), 5 (green; 202–207), and 4 (yellow; 172–177) overhang the active site (shown by the presence of substrate (red) of the PTEs).

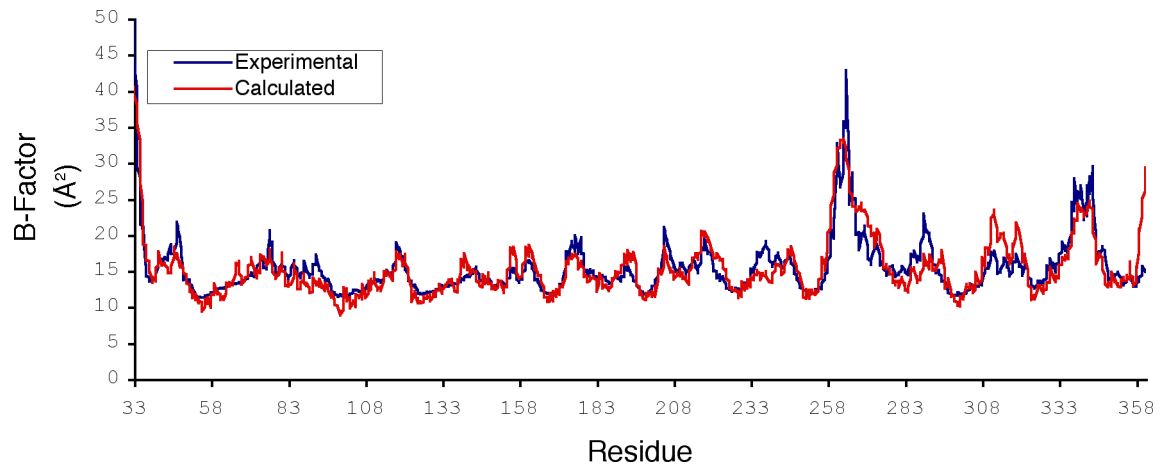


Fig. S3. Experimental vs. computational B factors. Correlation between experimental B factors (blue) and calculated B factors from NMA of an ENM of wild-type *arPTE*. The correlation coefficient for these two datasets was calculated and found to be 0.86.

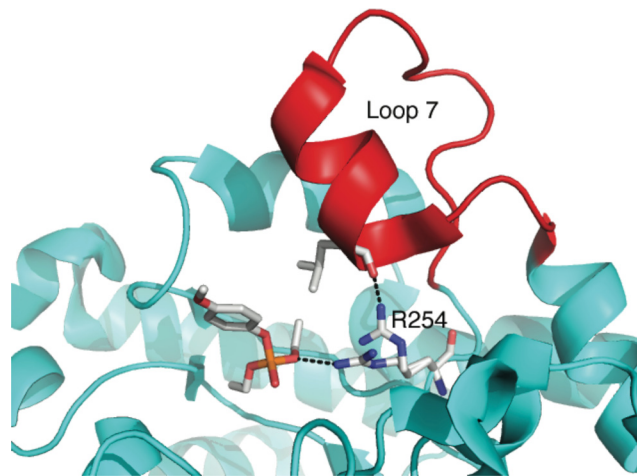


Fig. S4. Multiple conformations of R254. Arginine 254 in the *pd*PTE H254R mutant (1QW7) and in wild-type *ar*PTE (2R1N) adopts two major conformations, one of which can interact with the substrate, whereas the other forms a hydrogen bond with the backbone carbonyl of L271 of loop 7. This interaction is presumably responsible for the ca. 3-fold reduction in the *B* factor of this loop in *pd*PTE H254R, relative to the rest of the protein, compared with the wild-type enzyme.

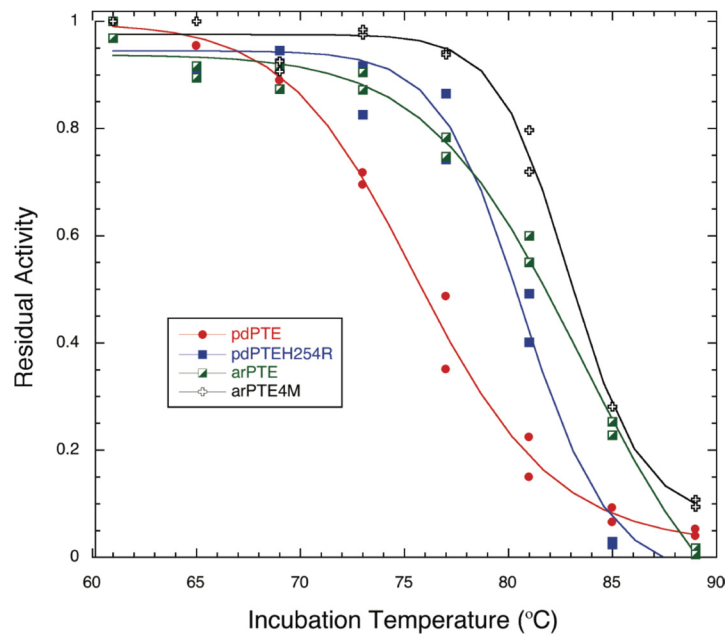


Fig. S5. Stability plots. Plots of residual activity versus incubation temperature for *arPTE*, *arPTE* 4M, *pdPTE*, and *pdPTE* H254R. It is clear that the presence of R254 in *arPTE*, *arPTE* 4M, and *pdPTE* H254R results in greater thermal stability. The thermal stabilities of the variants tested in this work was measured by determining the residual activity at 20 °C (at a concentration of 200 μ M paraoxon) after incubation of the protein at a series of temperatures for 15 min. The relative activities were plotted, and the temperature at which half of the original activity remained (T_{50}) was estimated using by fitting a curve to the following equation:

$$y = y^{\min} + \frac{(y^{\max} - y^{\min})}{1 + e^{\frac{(T - T_m)}{\lambda}}}$$

where y^{\min} and y^{\max} are the values of the minimum and maximum activities, T is the temperature of preincubation, T_m is the melting temperature, and λ denotes the slope of the curve within T_m . Melting points (T_{50}) of the variants studied are as follows: *pdPTE*, 76 °C; *pdPTE* H254R, 81 °C; *arPTE*, 84 °C; and *arPTE* 4M, 83 °C.

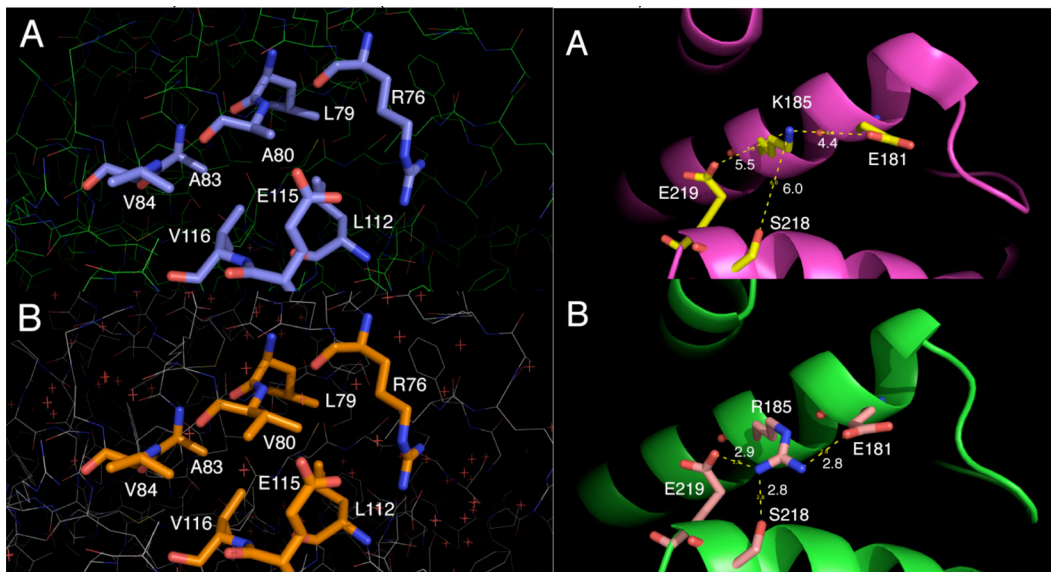


Fig. S6. The stabilizing mutations. (*Left*) The A80V mutation (3A3W) is shown to fill a surface cavity formed by V84, A83, L79, R76, L112, E115, and V116. (*Right*) The stabilizing K185R mutation (3A3W) is shown to result in the formation of up to three new bonds (with E181, S218, and E219).

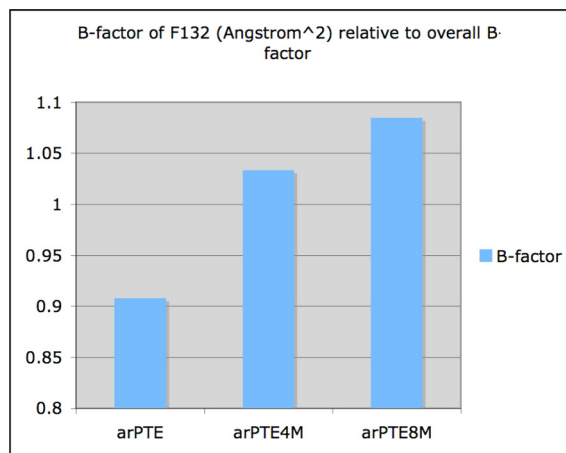


Fig. S7. *B* factor of F132 relative to the overall *B* factor. It is clear that in *arPTE* 4M and 8M, in which mutations at Q206P and D208G result in the loss of hydrogen bonds to the 170–174 loop, the *B* factor of F132, when modeled at full occupancy in the closed state, is significantly higher—corresponding to reduced occupancy. This finding is consistent with these mutations affecting the conformational distribution of F132.

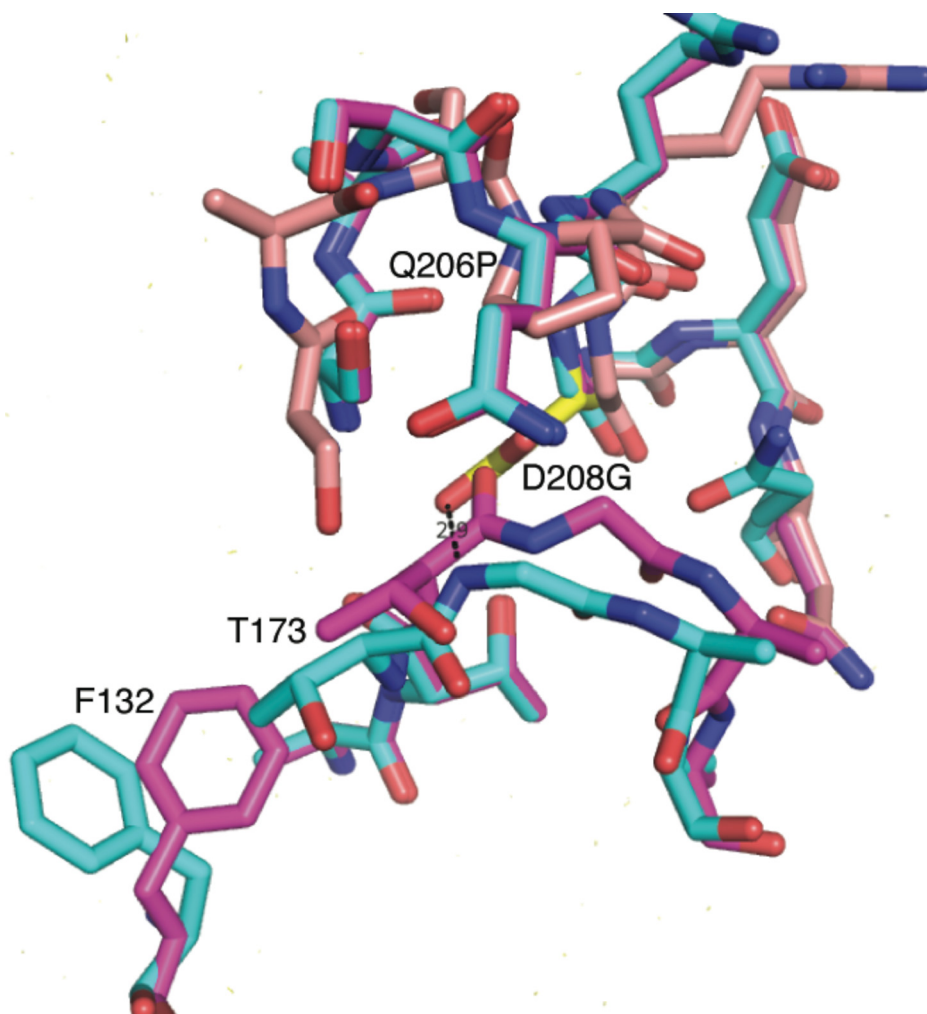


Fig. S8. The effects of D208G and Q206P on the multiple conformations of F132. As shown here, the flipping of F132 from the closed (aqua) to the open (magenta) conformations (3A4J) requires a shift in loop 4, in order for movement of T172 to provide space. The D208G mutation (yellow; 3A4J) results in the loss of a hydrogen bond contact between loop 5 and loop 4 (T173), as well as the loss of steric hindrance, to facilitate this movement. Similarly, the Q206P mutation (pink; 3A3W) results in a kink of loop 5, again providing room for loop 4 to adopt a second, open, conformation.

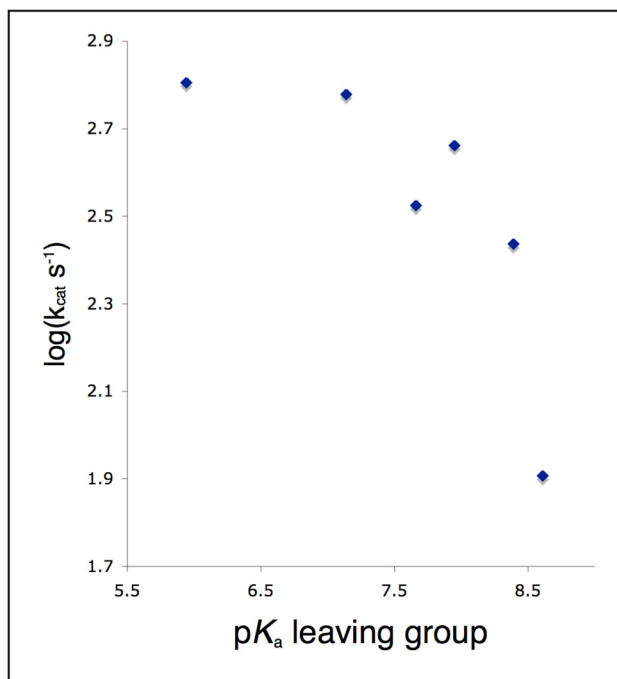


Fig. S9. Brønsted plot of *pdPTE* H254R. Brønsted plots of *pdPTE* and *pdPTE* H254R were made by assaying the turnover of a series of substrates with leaving groups with different $\text{p}K_{\text{a}}$ values. The plot reveals a biphasic dependence on the leaving group $\text{p}K_{\text{a}}$, consistent with a change in the rate-determining step from bond hydrolysis to a physical effect. Substrates used include 3-fluoro 4-dinitrophenyl diethyl phosphate ($\text{p}K_{\text{a}}$ 5.94), 4-nitrophenyl diethyl phosphate ($\text{p}K_{\text{a}}$ 7.14), 4-diethyl phosphate benzaldehyde ($\text{p}K_{\text{a}}$ 7.66), 4-cyanophenyl diethyl phosphate ($\text{p}K_{\text{a}}$ 7.95), and 3-nitrophenyl diethyl phosphate ($\text{p}K_{\text{a}}$ 8.39) [Khersonsky O, Tawfik DS (2005) *Biochemistry* 44:6371–6382].

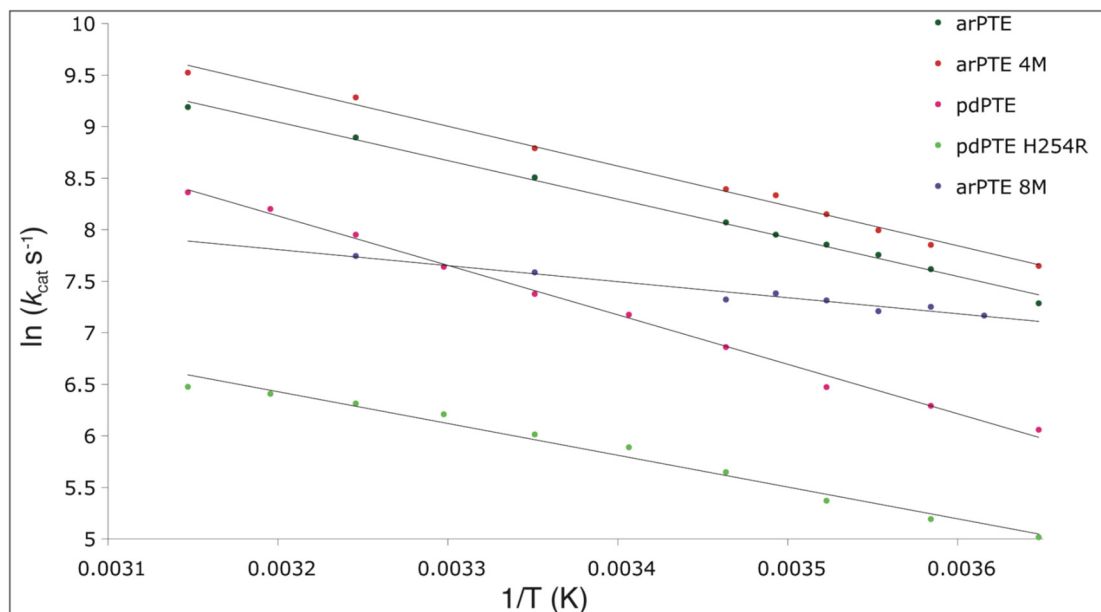
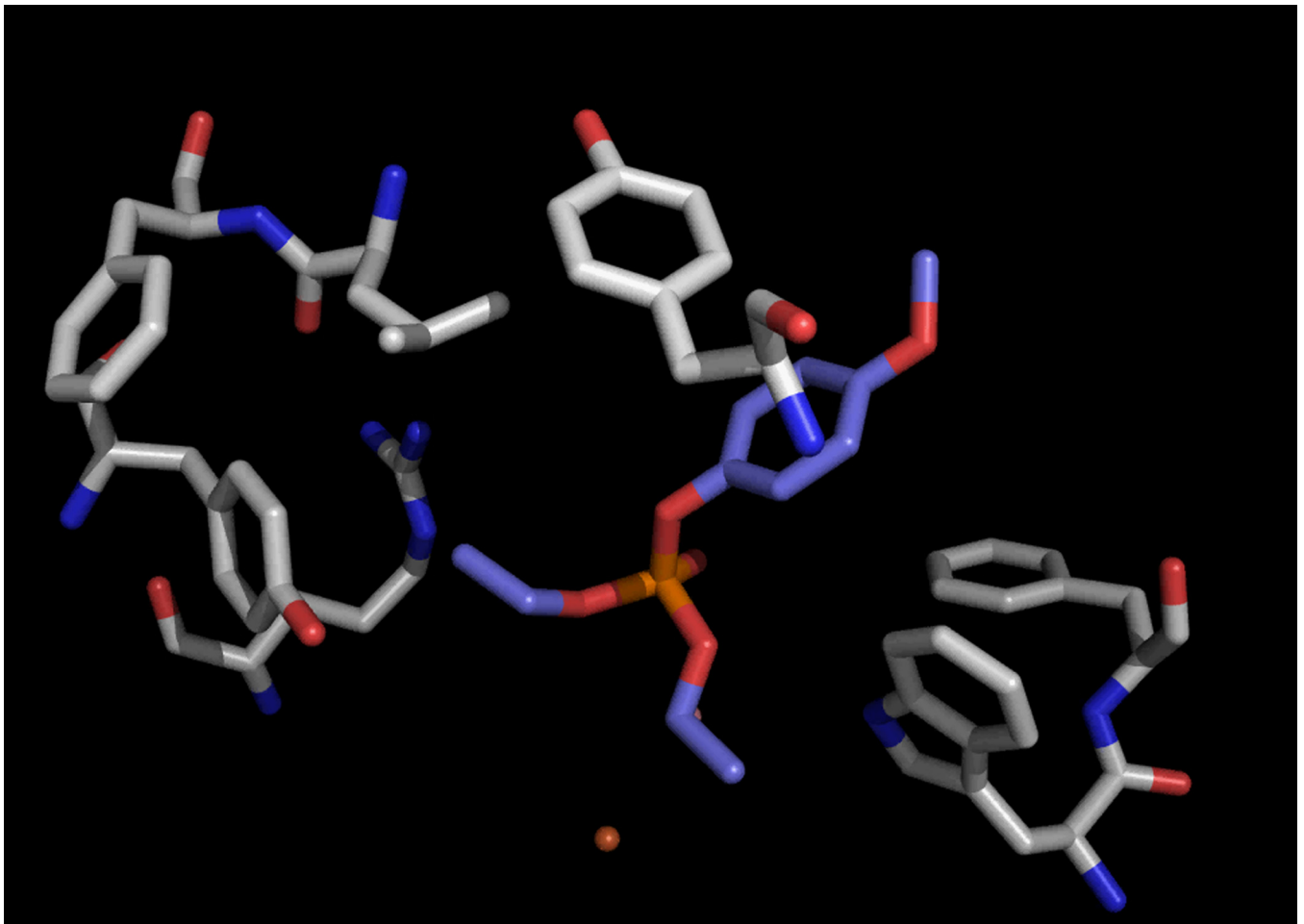
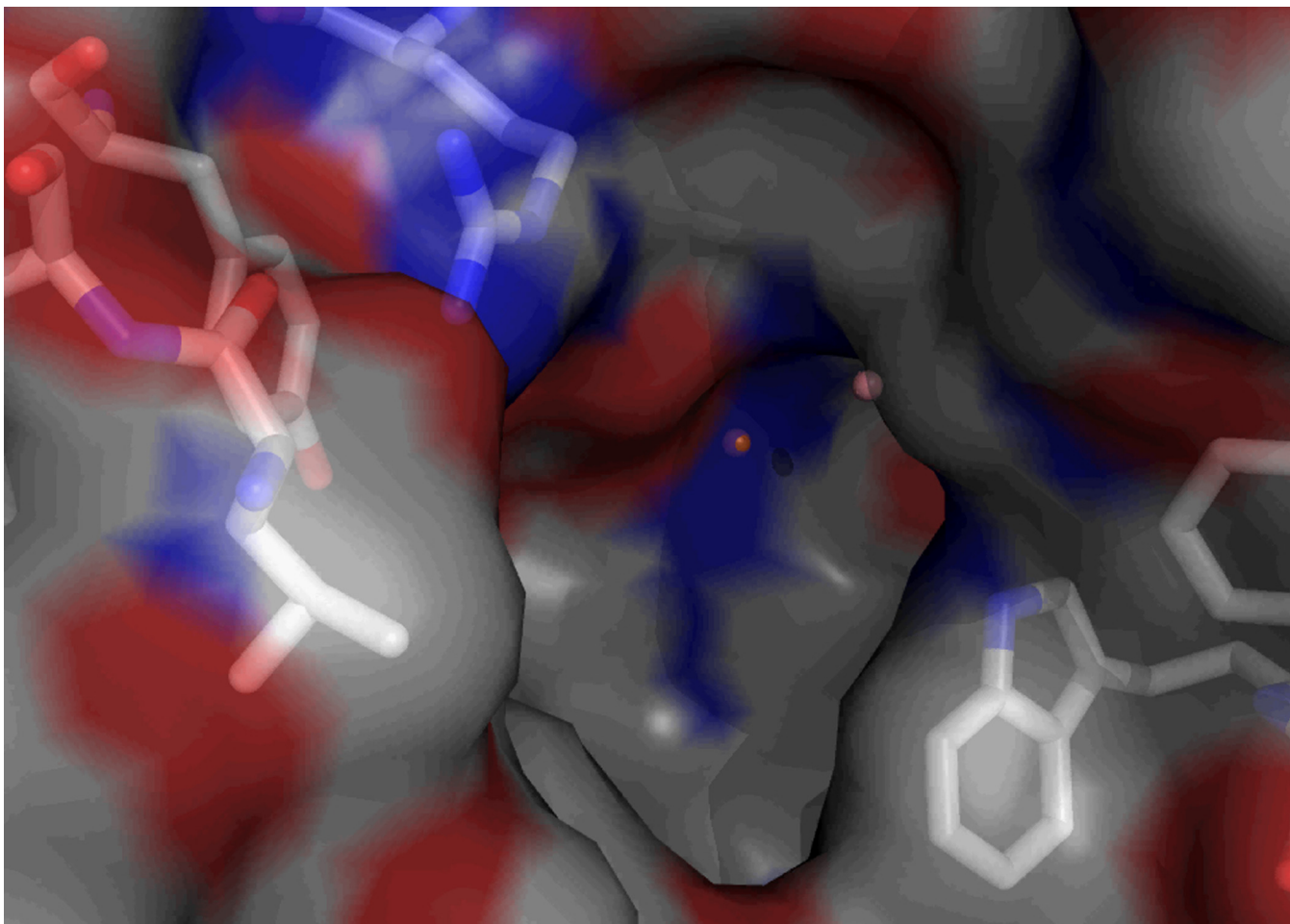


Fig. S10. Arrhenius plots of the five PTE variants. Arrhenius plots were made by determining the kinetic parameters at a range of temperatures between 278.15 and 323.15 K. The temperature of the reaction was controlled using PCR thermocyclers (Bio-Rad), and the reactions were monitored after 5 min using 96-well plate readers (Labsystems Multiskan Ascent). Less than 20% substrate was hydrolyzed. The activation energy was calculated using the following equation: $\ln k = A + E/R.T$, where k equals the rate per second, A equals the preexponential factor, E equals the activation energy, R equals the gas constant (8.314 J/mol K), and T equals the temperature. From this the activation entropy was calculated using the following equation: $A = e^{S/R} \cdot k_B \cdot T \cdot e/h$, where A equals the preexponential factor, S is the activation entropy, R is the gas constant, k_B is the Boltzmann constant, h is Planck's constant, and T is the average temperature.



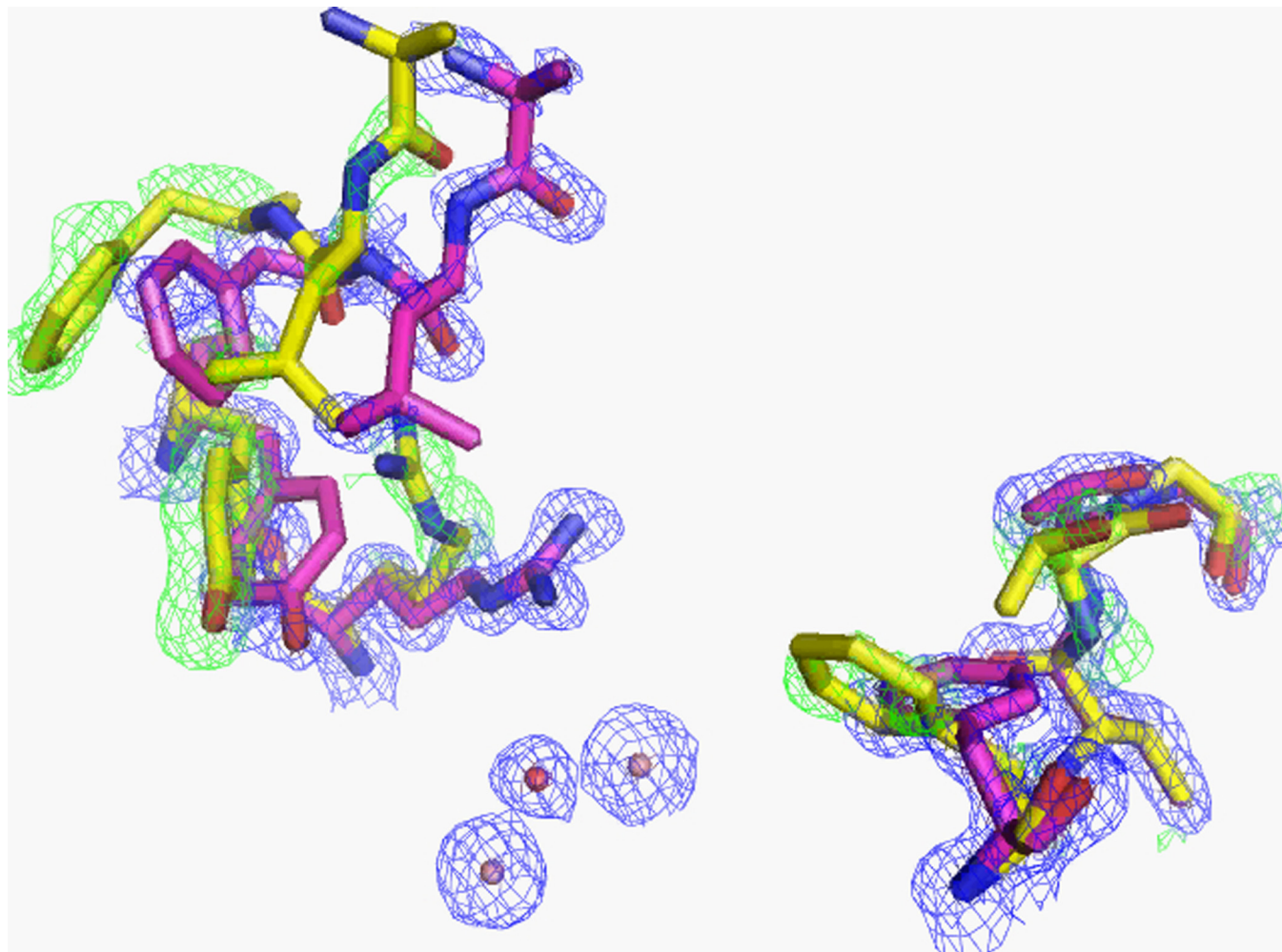
Movie S1. A morph between the substrate bound E_{open} (3A3W) and E_{closed} (2R1N) states of arPTE made using the Yale Morph server. [Krebs WG, Gerstein M (2000) *Nucleic Acids Res* 28:1665–1675].

[Movie S1 \(MOV\)](#)



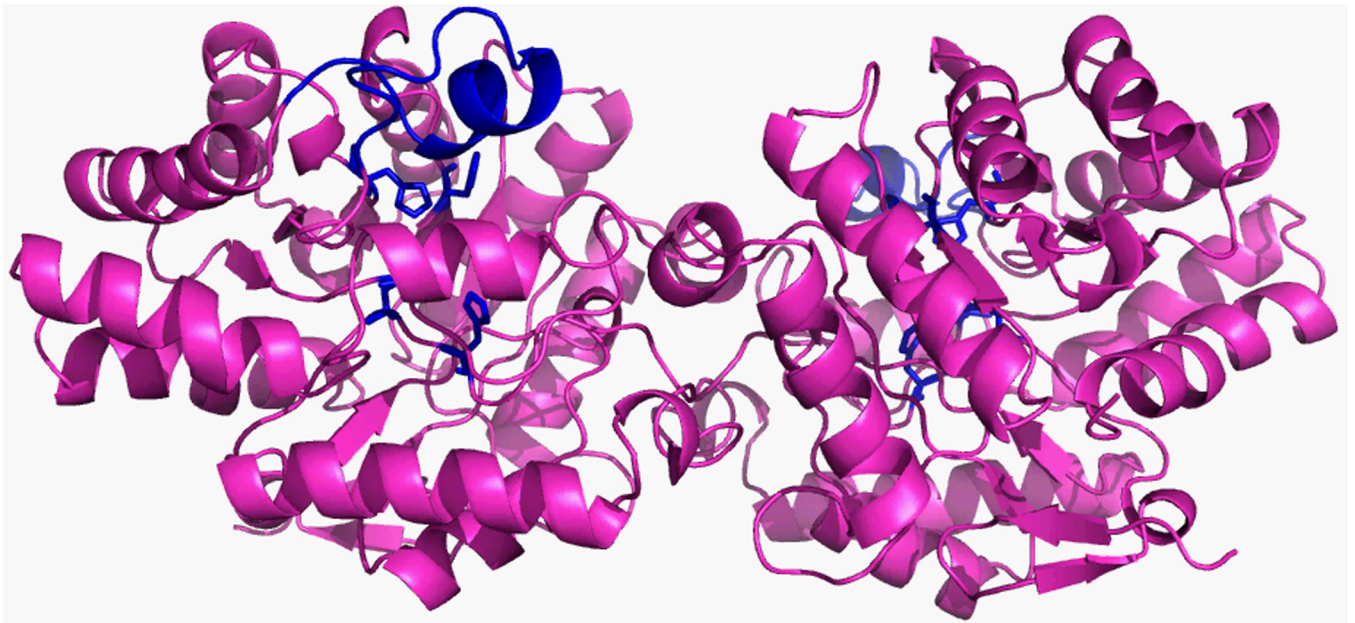
Movie S2. A morph between the substrate bound E_{open} (3A3W) and E_{closed} (2R1N) states of arPTE made using the Yale Morph server. [Krebs WG, Gerstein M (2000) *Nucleic Acids Res* 28:1665–1675], in which the substrate is not shown and the molecular surface is illustrated.

[Movie S2 \(MOV\)](#)



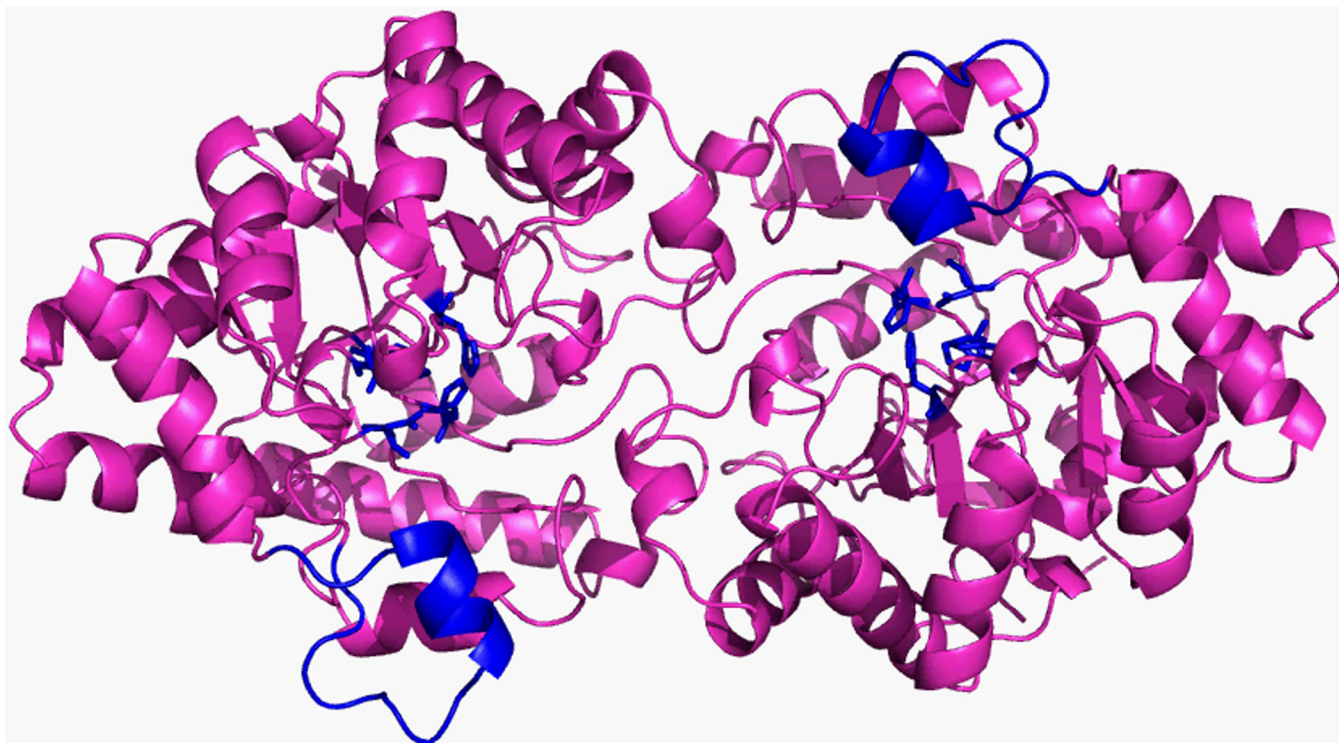
Movie S3. Multiple conformations exist within a single crystal structure. The structure and electron density is of *arPTE 4M* (3A4J). 2Fo-Fc density is colored blue (contoured at 1.5); Fo-Fc density is colored green (contoured at 3.0). This shows residues R254, Y257, L271, and F272 adopt a secondary open conformation on one side of the active cleft whereas F132 and T173 also adopt a secondary open conformation on the opposite side.

[Movie S3 \(MOV\)](#)



Movie S4. Illustration of the lowest frequency normal mode that involves movements of pseudorigid bodies within arPTE. The arPTE dimer is viewed from the side, active site residues are shown in blue as sticks, loop 7 is also colored blue.

[Movie S4 \(MOV\)](#)



Movie 55. Illustration of the lowest frequency normal mode that involves movements of pseudorigid bodies within *arPTE*. The *arPTE* dimer is viewed from above, active site residues are shown in blue as sticks, loop 7 is also colored blue.

[Movie 55 \(MOV\)](#)

Table S1. Data collection and refinement statistics for PTE structures

Crystal	arPTE 4M	arPTE 8M – EPO	arPTE 8M + EPO
Space group	P3121	P3121	P3121
PDB ID	3A4J	3A3X	3A3W
Unit cell parameters, Å	a = 108.95, c = 62.88	a = 109.16, c = 62.69	a = 109.01, c = 62.69
Data collection			
Resolution (Å)*	35.7–1.25 (1.28–1.25)	40.0–1.70 (1.76–1.70)	40–1.70 (1.76–1.70)
Unique reflections	118,492	47,531	43,843
Redundancy	11.0 (3.1)	10.3 (7.4)	9.5 (3.1)
$\langle I/\sigma(I) \rangle$	5.7 (3.3)	39.9 (6.0)	25.5 (1.7)
Completeness (%)	93.9 (63.8)	99.9 (99.1)	92.4 (51.9)
R_{symm} (%) [†]	6.0 (21.5)	5.3 (24.7)	7.8 (40.6)
Refinement			
No. reflections work/free	105,537/5,620	45,190/2,316	34,885/1,715
Resolution range	30.0–1.25 (1.28–1.25)	40.0–1.70 (1.74–1.70)	29.8–1.85 (1.90–1.85)
$R_{\text{work}}/R_{\text{free}}$ (%) [‡]	12.7/14.4 (20.2/23.9)	17.6/19.6 (22.7/28.0)	17.4/20.9 (25.9/33.9)
Rms deviations			
Lengths, Å	0.030	0.11	0.017
Angles, °	2.59	1.43	1.62

*Values in parenthesis are for the highest-resolution shell.

[†] $R_{\text{symm}} = \frac{\sum_{hkl} \sum_i |I_i(hkl) - \langle I(hkl) \rangle|}{\sum_{hkl} \sum_i I_i(hkl)}$ where $\langle I(hkl) \rangle$ is the average intensity of i symmetry-related observations of reflections with Miller indices hkl .

[‡] $R_{\text{work}} = \frac{\sum_{hkl} |F_{\text{obs}} - F_{\text{calc}}|}{\sum_{hkl} F_{\text{obs}}}$; 5% of the data that were excluded from the refinement were used to calculate R_{free} .